


Evaporation and Rheology Chart the Processability Map for Centrifugal Force Spinning

Jorgo Merchiers,^{||} Carina D. V. Martínez Narváez,^{||} Cheryl Slykas, Naveen K. Reddy,^{*} and Vivek Sharma^{*}

 Cite This: *Macromolecules* 2021, 54, 11061–11073

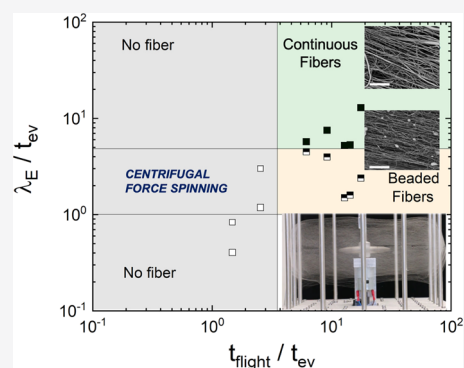
 Read Online

ACCESS |

 Metrics & More

 Article Recommendations

ABSTRACT: We show that poly(ethylene oxide) (PEO) solutions formulated using solvent mixtures of acetonitrile (AcN) and water can be centrifugally spun into fibers. We find that spinnability and fiber morphology depend on solvent choice if polymer concentration, solution shear rheology, the number of entanglements, extensional relaxation time, and the parameters for centrifugal spinning are nearly matched. We obtain an intrinsic spinnability map for volatile entangled (VE) polymer solutions by contrasting the measured shear relaxation time with the evaporation rate determined using thermogravimetric analysis (TGA). Finally, we chart a processability map for centrifugal spinning by plotting extensional relaxation time, measured for the volatile polymer solutions using a closed-cell dripping-onto-substrate (DoS) rheometry, against the time of flight (from the nozzle to the collector) by scaling both the timescales with an evaporation time. The processability map incorporates the influence of centrifugal spinning speed, nozzle diameter, distance from the collector, ambient conditions, and solvent and polymer properties, establishing an imitable paradigm for distinguishing between spinnable and sprayable formulations.



INTRODUCTION

Centrifugal force spinning (CFS) has fast emerged as a method for producing continuous fibers or filaments from polymer solutions and melts, often with additives that enhance the functionality of resulting nonwoven structures.^{1–3} Cotton candy as a product highlights the ease, rate, flexibility, and allure of this fiber/nonwoven manufacturing process and its scalability. Many recent studies focus on centrifugal spinning polymer solutions^{4–7} to take advantage of room-temperature processing and the possibility of producing finer fibers without the need for superfine nozzles, melt-processable polymers, and methods like electrospinning that require high-voltage sources and work with a limited range of solvents.^{1,4,8,9} However, a combination of complex free surface flow and instabilities, non-Newtonian fluid properties that change due to evaporation or solidification, mass or heat transfer (often both), as well as polymer stretching, orientation, and crystallization accompany the formation of centrifugally spun fibers.^{10–13} The coupling of multiple transport processes and non-Newtonian fluid mechanics present formidable challenges to creating a CFS processability map and connecting spinnability, heuristically identified with the ability to make fibers, with the choices of process and material parameters. Several theoretical and simulation studies probe the influence of non-Newtonian rheology and fluid mechanics in dictating the initiation, extension, and thinning of the spiraling jet from a fast-rotating

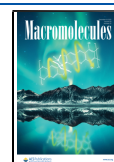
spinneret or nozzle, the role of viscoelastic free surface flows and instabilities, and the influence of evaporation or solidification process.^{10–14} The significant impacts of process parameters like spinning speed, nozzle shape and size, distance to the collector and airflow, and varying polymer concentration and molecular weight on fiber diameter and morphology are tabulated and discussed in several experimental and theoretical studies.^{1,4–7,10–18} However, fundamental questions remain about the impact of solvent choice, through the influence on rheological response, especially to extensional flows and evaporation, in dictating spinnability, motivating this study.

Here, we highlight the influence of changing solvent properties on spinnability and final fiber morphology under matched processing conditions by formulating the spinning dopes as solutions of 3 and 5 wt. % PEO in acetonitrile (AcN) and water mixtures. Variation in AcN weight fraction influences the volatility, surface tension, density, viscosity, dielectric constant, and polymer–solvent interactions. Several centrifugal force spinning (CFS) (and likewise, electrospinning

Received: August 26, 2021

Revised: November 8, 2021

Published: November 22, 2021



(ES)) studies have explored the influence of the solvent choice on the morphology of fibers formed by poly(ethylene terephthalate) (PET), poly(vinyl pyrrolidone) (PVP), polylactide (PLA),^{13,18–20} and PEO fibers.^{21–23} Still, the use of neither electrospinning nor CFS is described before for making fibers from PEO solutions formulated in AcN/H₂O solvent mixtures. The choice of PEO solutions is motivated by three factors. First, the formation, morphology, and properties of PEO fibers are the focus of many fundamental studies.^{1,3,5,10,15,24–38} Second, fibers formed by PEO alone, using PEO to enhance spinnability, or containing PEO blended with other polymers, particles, or proteins, are considered suitable for applications ranging from drug delivery, antimicrobial filters, battery separators, photovoltaics, and separation membranes.^{24,25,30,35–41} Third, we have extensively characterized shear and extensional rheology response of aqueous PEO solutions,^{42–46} and we recently showed that PEO fiber mats centrifugally spun with entangled PEO solutions in pure AcN rival crystallinity and mechanical properties of electrospun PEO fibers.³²

This paper identifies and discusses the timescales for solvent loss and fiber formation, compared to several intrinsic timescales in the problem, to construct a processability map. The time of flight from the nozzle to the collector depends on the rotational rate, the distance between the collector and the spinneret, and the trajectory of the spiraling jet. It can be compared to (liquid) jet-fiber (solid) transformation time, t_{jf} . For solution-CFS, the molecular diffusion within the drying polymer solution jet and hydrodynamic processes that assist in solvent vapor removal from fiber surface set the evaporation-based time, t_{je} . In melt-CFS, the phase transition kinetics due to cooling below crystallization and glass-transition temperatures set solidification-based time, t_{fm} , and in reactive CFS, polymerization reaction kinetics determine the reaction-limited time, t_{fr} .^{15,16} The spiraling liquid jet undergoes drawing and thinning primarily under the influence of stresses contributed by inertia, centrifugal forces, capillarity, viscoelasticity, and aerodynamic drag.^{10–13,18} The interplay of different stresses can drive or delay the formation and growth of a capillarity-driven instability that must be controlled and understood to obtain continuous fibers rather than drops. The challenges in quantifying nonlinear rheology, non-Newtonian fluid mechanics, and pinching dynamics that influence dispensing of rheologically complex fluids led Clasen et al.⁴⁷ to christen a potential processability map, “a map of misery”. However, the fiber formation from polymer solutions additionally involves mass transfer considerations, though concentration-dependent and humidity-influenced phase behavior can also play a role. A review of theoretical models of CFS or ES (or any fiber spinning techniques)^{9–14,18,48,49} and previous attempts at describing spinnability or stringiness^{9–15,18,48–52} presents us with a formidable array of parameters appearing in coupled, intricate transport equations, with additional nonlinearities introduced by viscoelasticity, free surfaces, and evaporation from mobile jets.

Here, we set ourselves the task of abstracting, charting, and presenting a pragmatic and easily computable processability map based on the timescales that can be measured experimentally and estimated theoretically in a straightforward manner. We characterized the shear rheology response using torsional rheometry and identified the unentangled and entangled regimes by examining the concentration-dependent variation in zero shear viscosity. We obtained a measure of

shear relaxation time from the onset of shear thinning and determined the extensional relaxation time using dripping-onto-substrate (DoS) rheometry.^{42–45,53,54} The magnitude and concentration-dependent variation of the measured extensional relaxation time, λ_E is usually distinct from the shear relaxation time, due to the role of stretched chain hydrodynamics.^{42–46,55–66} The response to extensional deformations is relevant for fiber spinning and jetting or spraying applications. We opted for closed-cell DoS rheometry to minimize evaporation, as volatile-entangled (VE) polymer solutions exhibit substantial concentration-dependent variation in rheology. We also measured the evaporative mass loss as a function of time using thermogravimetric analysis (TGA). Finally, we show that plotting shear relaxation time against TGA-based evaporation rate produces an intrinsic spinnability map with sufficient contrast for identification of spinnable regime using CFS with matched processing conditions. Finally, we outline a pragmatic processability map that incorporates the influence of processing conditions and extensional rheology effects by choosing extensional relaxation time and time of flight scaled with relative evaporation time as coordinates.

MATERIALS AND METHODS

Poly(ethylene oxide) or PEO of molecular weight $M_w = 600$ kg/mol (Sigma-Aldrich) was dissolved in acetonitrile (AcN) solvent (HPLC grade, VWR chemicals) under mild mixing conditions, as long flexible chains are known to be prone to chain scission. The molecular weight of PEO was checked before and after mixing, and no differences were observed. We spun PEO fibers using a bespoke centrifugal force spinning (CFS) setup designed at Hasselt University with the flexibility for changing nozzle type and material and with shifting and lifting mechanisms that allow control over nozzle–collector distance.^{17,32} The influence of nozzle properties and rotational speed on fiber formation and morphology is detailed in a previous contribution.¹⁷ We centrifugally spun fibers for a range of PEO concentrations with matched processing parameters like rotational speed (4000 rpm), temperature (298 K), distance to the collector (12 cm), and nozzle diameter (0.6 mm). The SEM images were acquired using a ZEISS Gemini 450 (Zeiss, Zaventem, Belgium). The fiber diameter and standard deviation were analyzed in ImageJ. Mass loss as a function of time for the polymer solutions as measured using thermogravimetric analysis (TGA) using Q50 apparatus (TA Instruments, New Castle, DE) at a fixed temperature of 25 °C and under a nitrogen atmosphere, with a flow rate of 90 mL/min. The steady shear viscosity was characterized using cone-and-plate geometry (50 mm diameter, 1° cone angle) on an Anton Paar MCR 302 Rheometer (torque range 10^{−5}–200 mN·m), and we checked that the polymer solutions utilized on both sides of the Atlantic had similar shear rheology response. The steady shear viscosity, $\eta(\dot{\gamma}) = \tau_{12}/\dot{\gamma}$ was calculated from the measured shear stress, τ_{12} from imposed shear rates in the range of $\dot{\gamma} = 0.01$ –10³ s^{−1}. The temperature was maintained using a Peltier element, and we used a solvent trap to minimize the influence of solvent evaporation on the measurements.

We characterized the extensional rheology response of the PEO solutions using dripping-onto-substrate (DoS) rheometry. A finite volume of fluid is dispensed through a stainless-steel nozzle and is deposited on a clean glass substrate at a height H below the nozzle. The nozzle radius is kept constant for all experiments for the PEO solutions with outer diameter, $2R_0 = 2.108$ mm and an inner diameter, $D_i = 1.6$ mm. The fluid is pumped at a low and fixed flow rate ($Q = 0.02$ mL/min) and an aspect ratio of $H/D_0 \approx 3$. The imaging system includes a light source, a diffuser, a high-speed camera (Fastcam SA3 with a Nikkor 3.1× zoom (18–25 mm) lens), and an attached macro lens to improve magnification at the frame rates used (8000–25 000 frames per second). The DoS videos are analyzed with ImageJ and specially written MATLAB codes to determine the minimum neck

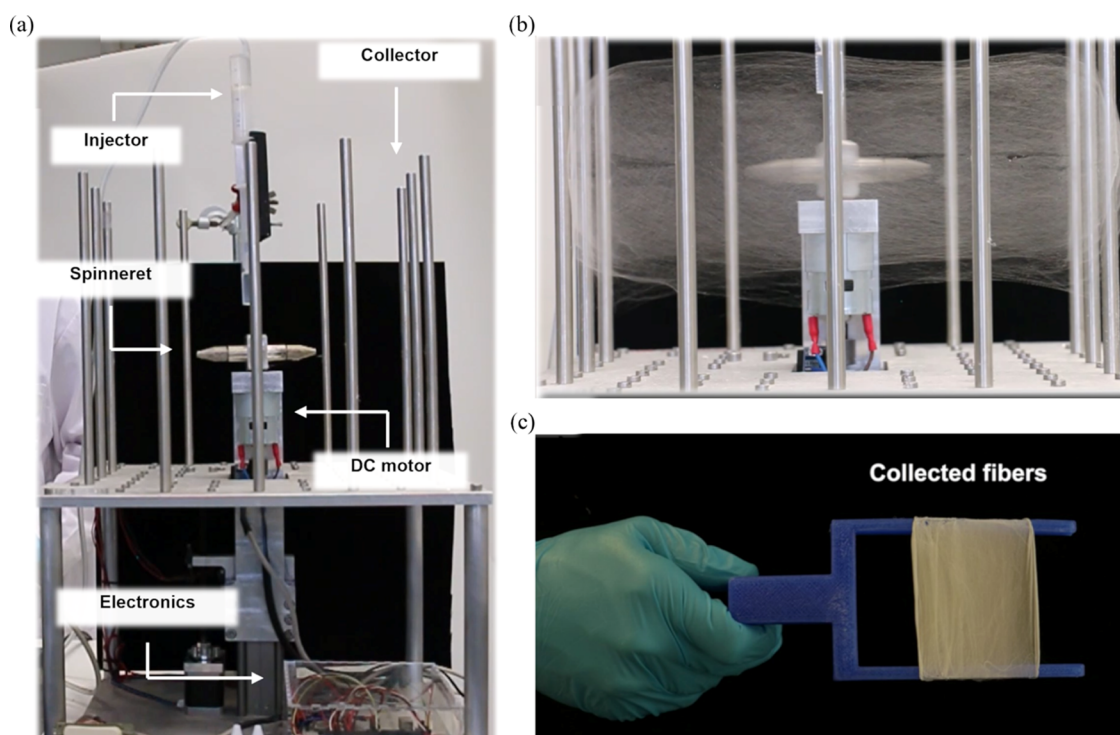


Figure 1. Centrifugal force spinning apparatus used for preparing PEO fiber mats. (a) Photograph of the homebuilt centrifugal force spinning or rotary jet spinning setup. The labels mark the critical parts of the apparatus, including an injector, a spinneret, a DC motor, and the electronics that allow control over the rotational speed. (b) Snapshot showing the fiber spinning process that deposits continuous fibers on the collectors. (c) Image showing an example of a fiber mat formed with the collected fibers.

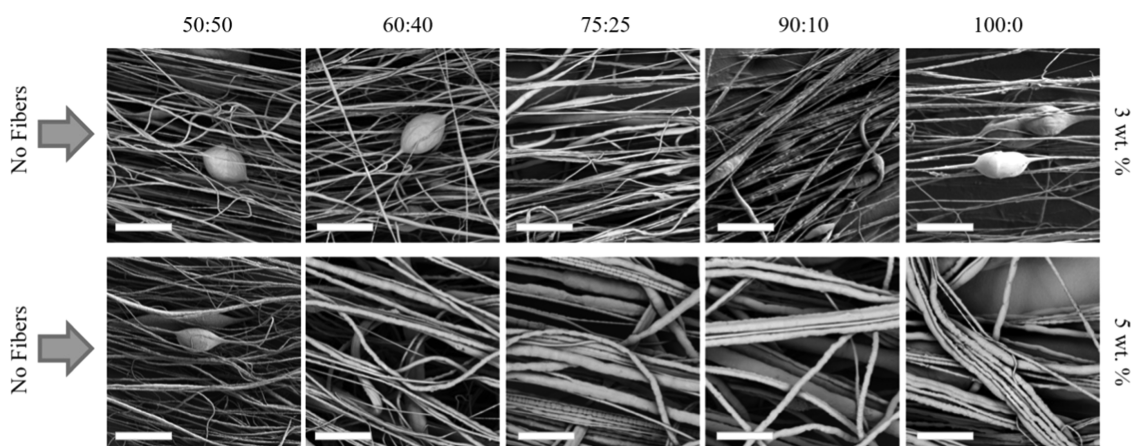


Figure 2. SEM images of the centrifugally spun PEO fibers. In each row, the concentration of AcN added to the solvent mixture increases from left to right, and no fibers form for solvent mixtures with <50 %AcN. In contrast, each column compares the influence of change in polymer concentration for the indicated mixed solvent. The scale bar is 20 μm .

radius as a function of time. The DoS rheometry setup, design considerations, specific advantages contrasted to other extensional rheology methods, and various approaches to analyzing datasets are detailed in our previous contributions,^{42–46,53,54,67–73} and in several recent studies.^{74–84} We used a closed transparent cell to carry out experiments in an atmosphere saturated with solvent vapor. Even though we find that evaporation exercises negligible influence for unentangled aqueous solutions, a closed cell is needed for volatile-entangled (VE) polymer solutions that display strong concentration-dependent change in rheology.

RESULTS AND DISCUSSION

Centrifugal Force Spinning of PEO Fibers from AcN/H₂O Solutions. A homebuilt centrifugal fiber spinning setup,

included in Figure 1a as a labeled photograph, was used to produce fibers from PEO solutions prepared in AcN/H₂O solvent mixtures. The setup consists of two symmetrically mounted nozzles, and the possibility to move pillars or raise base provides an adjustable collector-nozzle distance, as detailed previously.¹⁷ Figure 1b shows a snapshot highlighting the deposition process, whereas Figure 1c shows a fiber mat after collection. Fibers were centrifugally spun with matched processing parameters and similar environmental conditions. The rotational speed, collector distance, and nozzle diameter were set at fixed values of 4000 rpm, 12 cm, and 0.6 mm, respectively.

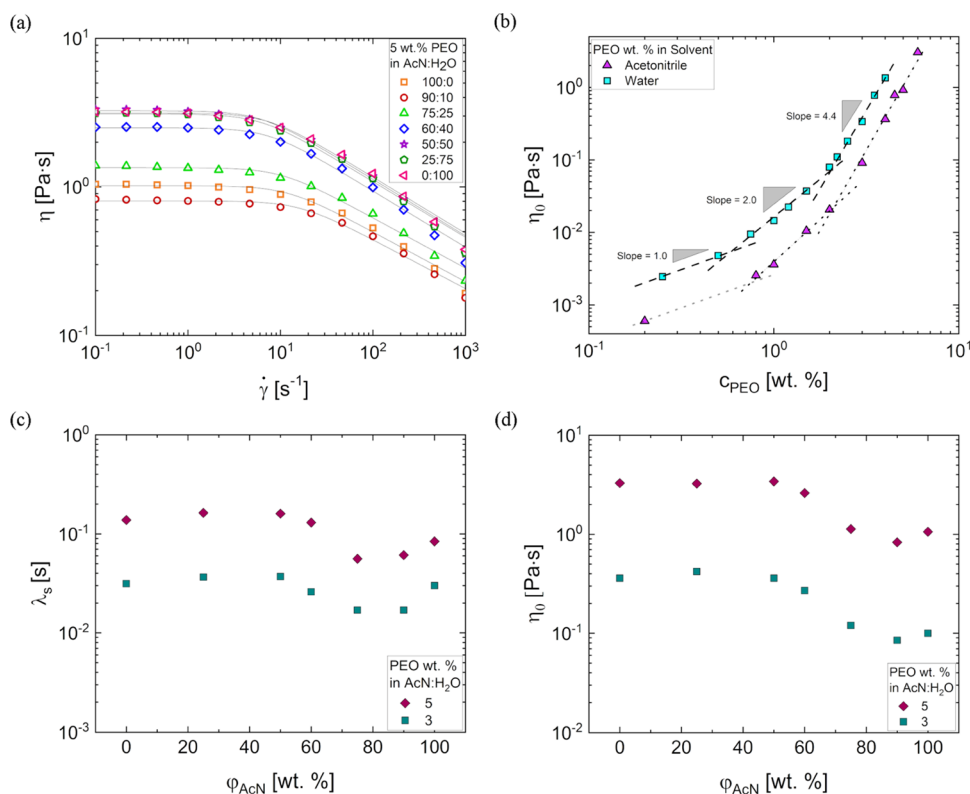


Figure 3. Influence of AcN fraction on shear rheology response of PEO solutions. (a) Steady shear viscosity as a function of shear rate for 5 wt. % PEO solutions displays an AcN weight fraction-dependent variation and shear thinning response. The Carreau model fits are shown as solid black lines. (b) Concentration-dependent increase in zero shear viscosity as a function of PEO in pure water showing larger values than pure acetonitrile solutions at matched concentrations. (c) Shear relaxation time and (d) zero shear viscosity of 3 and 5 wt. % PEO solutions as a function of AcN fraction in solvent mixtures display a nonmonotonic variation.

The centrifugal spinning of PEO solutions in pure acetonitrile produced a spray of droplets for $c < 2$ wt. %, beaded fibers for 2–3 wt. %, and continuous fibers for 4–6 wt. %. Centrifugal forces generated by the chosen processing parameters produce insufficient stress to create continuous jets for polymer concentration beyond 6 wt. %. Thus, the spinnability range of PEO/AcN solutions for centrifugal fiber spinning at 4000 rpm lies between 2 and 6 wt. %. We spun PEO solutions in AcN/H₂O solvent mixtures to evaluate solvent composition, which leads to a variation in material properties like surface tension, solvent viscosity, and vapor pressure, which impacts spinnability and fiber morphology. For this comparison, we used matched processing parameters like rotational speed (4000 rpm), temperature (298 K), distance to the collector (12 cm), and nozzle diameter (0.6 mm). Figure 2 shows SEM images of fibers obtained by centrifugal force spinning for $c = 3$ wt. % and $c = 5$ wt. % polymer solutions in four solvent mixtures as well as pure AcN as a solvent.

Solutions prepared in pure water yielded only a spray of droplets, whereas in pure AcN, continuous fibers form. No fibers form if the AcN fraction is below 50% of the solvent, few beads on the fiber web appear if PEO with $c = 3$ wt. % in 50, 60%, and pure AcN is centrifugally spun. The PEO solutions with 90:10 AcN/H₂O have a reduced bead formation, whereas the 75:25 solvent mixtures show a complete disappearance of beads. The fiber diameters of the 90:10 and 75:25 solvent compositions are comparable, but the 60:40 and 50:50 AcN/H₂O solvent mixtures show finer diameters. Solutions with 5 wt. % PEO show no fibers for AcN fraction below 50%, a few beads for 50:50 AcN/H₂O, and continuous fibers for solvent

mixture with AcN fraction equal to and above 60%. The fiber diameters appear comparable for the 90:10 and 75:25 solvent mixtures, and lower diameters appear for 60:40 and 50:50 AcN/H₂O. Assuming the differences are caused by rheology and evaporation effects, we made the measurements described next.

Steady Shear Viscosity and Relaxation Time of PEO in AcN/H₂O Solutions. Steady shear viscosity as a function of shear rate, $\dot{\gamma}$, is plotted in Figure 3a for 5 wt. % PEO solutions. The rate-dependent viscosity datasets, with a Newtonian plateau at a low shear rate followed by shear thinning response, observed at all concentrations (see solid black lines in Figure 3a), are captured using the Carreau model⁸⁵ expression

$$\eta(\dot{\gamma}) = \eta_{\infty} + \frac{\eta_0 - \eta_{\infty}}{(1 + (\dot{\gamma}/\dot{\gamma}_c)^2)^{(n-1)/2}} \quad (1)$$

Here, η_0 and η_{∞} correspond to the rate-independent zero shear viscosity and the infinite shear rate viscosity. Defining η_{∞} as equal to the solvent mixture viscosity reduces the total number of free parameters to three. The exponent n quantifies the power law dependence of the viscosity at intermediate shear rates, and a critical shear rate, $\dot{\gamma}_c$, captures the onset of the power law region that allows the computation of the shear relaxation time, $\lambda_c = \dot{\gamma}_c^{-1}$. Zero shear viscosity, η_0 , values as a function of PEO concentration in pure water and pure acetonitrile solutions are shown in Figure 3b. Aqueous PEO solutions exhibit higher viscosity than PEO in acetonitrile solutions at matched concentrations. Three regimes identified for the aqueous PEO solutions show $\eta_0 \propto c^k$ with $k = 1.0, 2.0,$

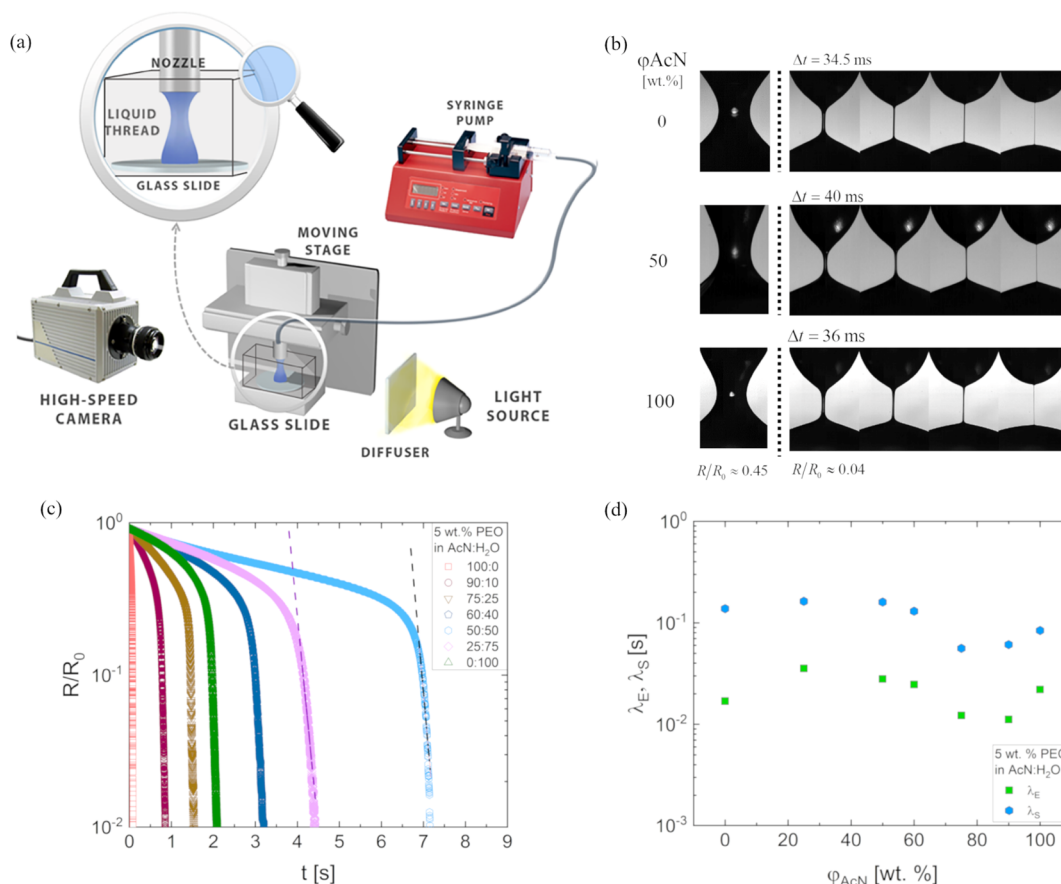


Figure 4. Pinching dynamics and extensional relaxation times of PEO in AcN/H₂O mixtures. (a) Dripping-onto-substrate (DoS) schematics include an imaging and dispensing system. DoS involves the visualization and analysis of an unstable liquid neck formed by a finite volume of fluid released onto a fixed substrate (zoomed-in image shows the closed cell). (b) Snapshots show neck shape evolution of 5 wt. % PEO in three AcN:H₂O/water mixtures. The first column corresponds to the neck shape at a matched $R/R_0 = 0.45$. The last three columns with time steps of 34.5, 40, and 36 ms for 0, 50, and 100 AcN content, respectively, highlight the slender cylindrical filament characteristic of an EC response. (c) Radius evolution data acquired using dripping-onto-substrate (DoS) rheometry plotted on a semilog scale show a pronounced elastocapillary regime and AcN concentration-dependent variation in the filament life span. (d) Extensional relaxation time as a function of the AcN fraction showing a nonmonotonic behavior that mimics the variation observed for shear relaxation time.

and 4.4. The respective three powers correspond to the dilute, semidilute, unentangled, and semidilute, entangled regimes.⁸⁶ Graphically, the entanglement concentration, $c_c \approx 1.8$ wt. %, appears to be comparable in both solvents, implying that 3 and 5 wt. % PEO solutions used in this study lie in the entangled regime.

Figure 3c,d, respectively, show apparent shear relaxation time, $\lambda_c = \dot{\gamma}^{-1}$, and zero shear viscosity values, extracted from the Carreau model fit to steady shear viscosity. Both η_0 and λ_c exhibit a nonmonotonic variation as a function of the AcN/H₂O ratio with a dip at 75:25 and 90:10. Previous studies attribute a similar dip to the changes in polymer conformation due to the variation of hydrogen-bonding interactions and preferential adsorption/hydration of PEO as a function of the water content in the binary mixtures.⁸⁷ Entangled PEO solutions in acetonitrile appear to form continuous fibers. In contrast, the entangled aqueous PEO solutions form a jet that splashes off the collector even though the zero shear viscosity of aqueous solutions is higher. Even though many studies on spinnability (mainly in electrospinning context) argue that spinnable solutions tend to form above entanglement concentration,^{88–91} our observations show that solutions with similar state of overlap and entanglements, as well comparable shear viscosity, can display dramatically distinct

spinnability and fiber morphology, implying that the role of extensional rheology and solidification process needs to be evaluated, as discussed in the following two sections.

Extensional Relaxation Time of Entangled PEO Solutions. The setup for DoS rheometry is shown in the schematic included in Figure 4a. The DoS rheometry protocols rely on the visualization and analysis of capillarity-driven pinching dynamics of liquid necks, in analogy with other capillarity-based techniques, like Capillary breakup extensional rheometer (CaBER) and other stretched liquid bridges,^{92–100} dripping,^{56,101,102} or jetting-based rheometry.^{103–108} Figure 4b shows the neck shapes and shape evolution for three AcN/H₂O ratios. Three snapshots of the image sequence from the last stage before pinch-off exhibit the pronounced cylindrical filament shape. We contrast neck shapes observed at the same scaled radius at an early stage. Even though the shear viscosity of PEO solutions in pure water is higher than the pure AcN at matched concentrations, the overall filament life span appears to be longer in AcN-added solutions, requiring the use of specific time intervals for each solvent. The radius evolution plots in Figure 4c initially display a viscocapillary (VC) response with a linear decrease in neck radius, followed by an elastocapillary (EC) regime that shows an exponentially slow decay in the radius. The EC regime results from an interplay of

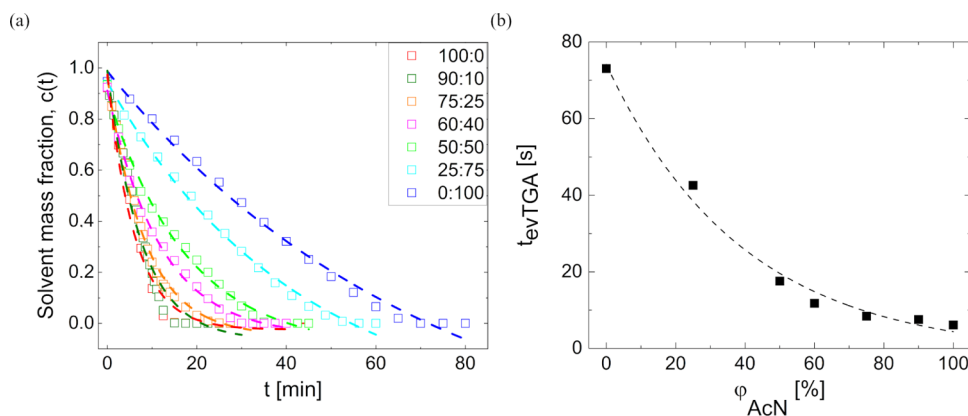


Figure 5. Mass loss and evaporation time are influenced by solvent choice. (a) Mass loss as a function of time (symbols) as measured using TGA (Q50 apparatus, TA Instruments, New Castle, DE) at a fixed temperature of 25 °C and under a nitrogen atmosphere. The dotted line fits an exponential decay function of the form $c(t) = A \exp(-t/t_{evTGA})$ to the mass loss data for 5 wt. % PEO solutions in different solvent compositions. (b) Evaporation time computed using TGA data, illustrating how the addition of AcN significantly decreases the solidification time compared to aqueous solutions.

capillarity and nonlinear viscoelastic stresses that arise in response to extensional flows associated with streamwise velocity gradients in the pinching necks. The simplest EC expression by Entov and co-workers that is rederived or discussed in studies based on the Oldroyd-B model^{55,103,106,109–114} uses the shear modulus, G and shear relaxation time, λ_s as parameters. It thus lacks due consideration of additional effects including non-Hookean elastic response, finite extensibility, and conformation-dependent drag that arise in response to strong flows for both unentangled and entangled solutions.^{43–45,61–66,85,94,115} Therefore, we use the following modified expression (introduced by Dinic and Sharma⁴⁴)

$$\frac{R(t)}{R_0} = \left(\frac{G_E R_0}{2\sigma} \right)^{1/3} \exp\left(-\frac{t - t_c}{3\lambda_E} \right) \quad (2)$$

as it accounts for the onset of EC at t_c and computes an apparent extensional modulus, G_E , distinct from the corresponding shear values.^{42–45,53}

The extensional relaxation time, λ_E , values measured for the 5 wt. % solutions, included in Figure 4d, correlate well with shear relaxation time, λ_s , and we find that chain dynamics and rheology are not influenced substantially by a change in AcN fraction. Furthermore, the extensional relaxation time $\lambda_E < \lambda_s$ for these entangled PEO solutions (both 3 and 5 wt. % solutions). The lower value of λ_E for entangled solutions is attributed to the influence of disentanglement and high stretch of the chains, contributed by non-Hookean elasticity, finite extensibility, and conformation-dependent drag.^{65,116–123} In contrast, dilute polymer solutions display $\lambda_E > \lambda_s$ attributed to the dramatic change in conformation, particularly for highly flexible, highly extensible polymers like PEO that can undergo coil stretch transition in response to extensional flow, leads to a longer extensional relaxation time, as detailed elsewhere.^{42–45,54–58,62,63}

As the unique advantages of DoS rheometry lie in facilitating the characterization of low viscosity (<100 mPa·s) and low-elasticity formulations (beyond the range of techniques), most of the published studies describe extensional relaxation time of unentangled polymer solutions.^{42–45,53,54,67,68,72–77,81} Even though a few DoS rheometry studies explore the extensional rheology of the entangled solutions of polysaccharides and

polyelectrolytes,^{45,54,67–69} there are no previous DoS rheometry studies of the entangled solutions of uncharged polymers, explored herein for the PEO solutions. However, the CaBER measurements carried out with aqueous PEO solutions also display $\lambda_E < \lambda_s$ values, in agreement with Figure 4b.⁹⁶ It is well-established that the knowledge of rate-dependent shear viscosity is not adequate to estimate or predict the strain- and strain-rate-dependent extensional viscosity (also referred to as tensile growth coefficient), $\eta_E = \eta_E^*(t, \dot{\epsilon})$ of even solutions and melts of bare polymers, and shear thinning polymer solutions can exhibit pronounced extensional hardening.^{42–45,52–54,64–68,74,75,94–99} Our preliminary studies using dripping-onto-substrate (DoS) rheometry protocols reveal that these entangled solutions also display strain hardening in response to extensional flows. A more detailed investigation of polymer concentration-dependent variation in shear and extensional rheology response for these PEO solutions in AcN/H₂O is underway. Therefore, here, we focus only on comparing the extensional relaxation time, and its relevance for assessing spinnability.

Evaporation Timescales of AcN/H₂O Solvent Mixtures. To contrast the differences in solvent loss over time in centrifugal spinning, we measured the mass loss from 30 mg of PEO solutions (with 5 wt. % polymer added) as a function of time using thermogravimetric analysis (TGA). The plots of mass loss as a function of time included in Figure 5a show that increasing the AcN fraction speeds up the solvent removal process. We can analyze the evaporation data using a simple mass transfer model that accounts for diffusion-limited mass transfer within the polymer solution and a boundary condition that incorporates the role of outside airflow using a mass transfer coefficient, as detailed in Sharma et al.^{124,125} While the model description becomes less realistic at later stages when the formation of polymer-rich shell impacts the diffusivity itself, the experimental datasets and plots include the effect of such a shell. Nevertheless, inspired by the simplified model,^{124,125} we fit the mass loss data with an exponential decay function and estimate an evaporation time, t_{evTGA} from the decay constant. The t_{evTGA} values obtained from TGA data are plotted in Figure 5b and include the influence of solvent diffusivity within the liquid layer and the mass transfer coefficient that depends on the flow velocity and material properties of the surrounding gas phase. Here, we used a

Table 1. Influence of Solvent Composition on Rheology and Evaporation

AcN fraction	η_0 [Pa·s]	λ_s [s]	λ_E [s]	t_{vc} [s]	Ec	t_{evTGA} [s]	$\frac{t_{evTGA}}{t_{evTGA,100}}$	De_s
100	1.06	0.084	0.022	0.018	4.6	6.15	1	0.0137
90	0.83	0.061	0.0112	0.014	4.3	7.55	1.23	0.0081
75	1.13	0.056	0.0122	0.019	2.9	8.42	1.37	0.0067
60	2.61	0.011	0.0247	0.045	2.9	11.8	1.92	0.0110
50	3.42	0.16	0.0280	0.059	2.8	17.6	2.86	0.0091
25	3.25	0.16	0.0355	0.049	3.3	42.6	6.93	0.0038
0	3.29	0.14	0.0169	0.028	4.9	73.1	11.9	0.0019

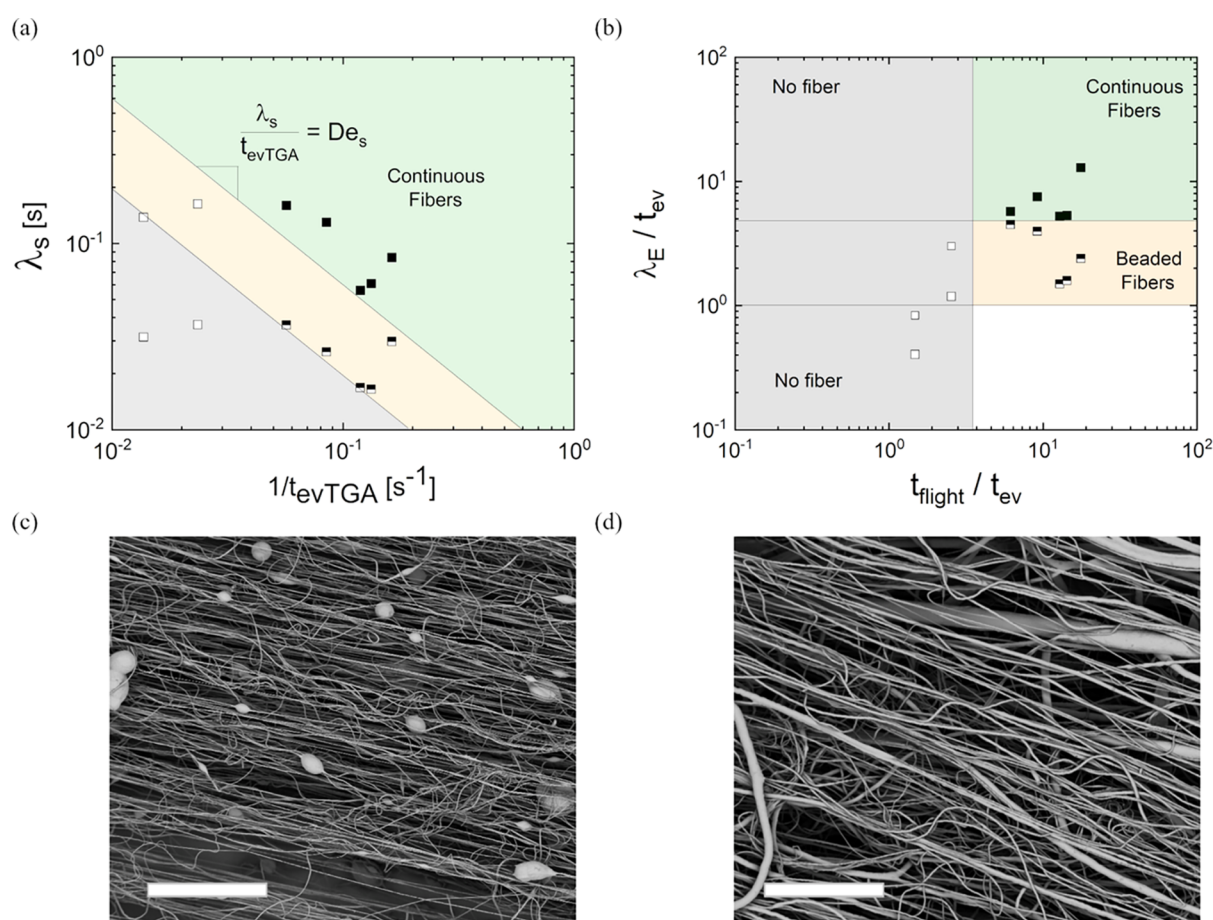


Figure 6. Intrinsic spinnability diagram and a processability map. (a) Shear relaxation time plotted against evaporation rate using the as-measured values obtained from the analysis of steady shear viscosity and mass loss via evaporation in TGA shows distinct regions of spinnable solutions above specific De_s values. (b) Comparison of three intrinsic timescales that capture the difference in evaporation time, relaxation time associated with viscoelasticity of the spinning drop, and time of flight set by processing conditions. Here, a processability map emerges with regions of continuous fibers self-selecting a quadrant with slower relaxation and faster evaporation. Open symbols: no fibers, half-filled: (c) beaded fiber mats and closed symbols: continuous fibers, as shown in (d). The scale bar is 100 μm .

nitrogen atmosphere and a flow rate of 90 mL/min. However, the measurement of solvent evaporation time using TGA involves no convective flow within the solution that can emulate flows that arise during fiber spinning and dispensing or coating processes. As the mass transfer coefficient depends on the sample geometry and ambient conditions (temperature, humidity, and gas velocity field), a suitable conversion factor is needed to determine mass loss during fiber spinning from TGA data. Additionally, during spinning, the rate of mass loss is influenced by changes in macromolecular conformation (stretching) and orientation. Nevertheless, the evaporation timescale extracted from TGA measurements (Figure 5)

characterizes the intrinsic differences in the evaporative loss of the solvent under matched conditions.

Processability Diagram Based on the Evaporation Timescale, Relaxation Times, and Time of Flight. The collection of fibers on the collector requires the formation of a stable spiraling jet that undergoes solidification before instability growth and before reaching the collector. The consideration leads to the identification of at least three crucial, relevant timescales: instability growth time, evaporation time, and time of flight. The growth of sinusoidal instability as well as pinching dynamics of necks of viscous fluids depends on the interplay of viscous stress and capillary pressure, with a characteristic time known as the viscocapillary time, $t_{vc} = \eta_0 D_0 /$

σ , and a dimensionless viscosity, expressed as Ohnesorge number, $Oh = \eta / \sqrt{\rho\sigma D_0}$, which is equal to the ratio of viscocapillary time, t_{vc} , to inertio-capillary time, $t_{ic} = \sqrt{\rho R_0^3 / \sigma}$.^{94,103,106,126} The intrinsic elastocapillary number, $Ec = \lambda_s \sigma / \eta_0 D_0 = \sigma / GD_0$, captures the influence of capillary stresses in comparison with elastic stresses on capillary-driven instability growth.^{94,127} Table 1 lists the values of these timescales and dimensionless groups obtained from the knowledge of shear rheology response and includes timescales obtained using evaporation rate (TGA) and extensional rheology (DoS) measurements. The values listed in Table 1 show that shear viscosity changes by nearly a factor of 3, and surface tension changes by almost a factor of 2. Hence, the resulting t_{vc} values remain roughly unchanged as the AcN fraction is varied. But as the relaxation time values change by no more than a factor of 2, the values of Ec also remain roughly unchanged as the AcN fraction is varied. Table 1 shows that only the evaporation rate shows a considerable variation as a function of the AcN fraction.

Several researchers have outlined processability maps by contrasting different timescales, length scales or forces in the problem. Ren et al.¹³ constructed an “operating diagram” using a plot of Oh against a Weissenberg number, $Wi = \lambda_s \dot{\gamma}$ (compares relaxation time to the timescale equal to the inverse of deformation rate). In contrast, Golecki et al.¹⁸ directly plotted centrifugal spinning RPM against viscosity values. However, our experimental results that show spinnability is quite different even if shear viscosity, relaxation time, and RPM are nearly matched, implying that both approaches are not suitable for evaluating spinnability as a function of solvent choice. Previously, Ren et al.¹³ discussed the correlation between the diameter of centrifugally spun fibers and this ratio, which they called an elasticity processability number ($P_e = \lambda_s / t_{evap}$). However, Ren et al.¹³ did not contrast these two intrinsic timescales to determine spinnability. Even though Golecki et al.¹⁸ discussed the role of evaporation, in their framework, matched viscosity and RPM lead to similar spinnability, in striking contrast with our observations. The “operating diagram” suggested by Fang et al. for reactive CFS,¹⁵ contrasts the timescale for UV-induced polymerization and the extensional relaxation time, λ_E along with time of flight. However, Fang et al.¹⁵ relied on adding a large molecular weight PEO to dramatically enhance λ_E . In contrast, Table 1 shows all solutions used here for a fixed PEO concentration have comparable values of λ_E that are proportional but slightly lower in magnitude, compared with the corresponding values of λ_s . However, the evaporation time appears to have a 12-fold variation and hence seems to induce the observed large variation in spinnability as a function of solvent composition.

Here, we postulate that to the first order, the intrinsic differences in the rheology and evaporation of these entangled polymer solutions can be characterized by the measured shear relaxation time, λ_s (see Figure 3d), and the evaporation timescale determined from TGA measurements, t_{evTGA} (Figure 5b), and are listed in Table 1. In Figure 6a, we plot the values of λ_s against $1/t_{evTGA}$ and we find that the continuous fibers appear above a critical value of the ratio of two timescales, which we call an intrinsic spinnability Deborah number, $De_s = \lambda_s / t_{evTGA}$. Here, we assume that the timescale over which the liquid jet develops an elastic shell in centrifugal spinning would show a similar trend as observed for t_{evTGA} . To obtain a pragmatic and minimalistic description, we proceed without

computing the conversion factor, expected to be a function of the processing conditions and macromolecular response. Hence, $De_s = 0.006$, shown as a dotted line, marks the boundary between different regimes. As the sample placed in a TGA pan has a film thickness ~ 0.4 mm, just a 10-fold decrease in thickness could shift this De_s value by 100-fold or more. Figure 6a shows that comparison of these two intrinsic timescales allows the creation of an intrinsic spinnability map such that lines corresponding to constant De_s values demarcate the transitions between beaded fibers and no fibers, and between beaded and continuous fibers. Such a spinnability map has not been discussed before.

However, after a careful examination of physicochemical processes underlying spinnability, we infer that it would be helpful to supplement the intrinsic spinnability map based on shear rheological and mass loss timescales measured with standard techniques, with a processability map, that explicitly accounts for the influence of time of flight that can be varied simply by changing spinning speed or nozzle–collector distance and accounts for extensional rheology response. We seek to draw a processability map that incorporates the influence of evaporation (solvent properties or ambient conditions), time of flight (RPM and nozzle–collector distance), and viscoelastic free surface flows (influenced by capillarity, elasticity, shear viscosity, and extensional rheology response). In Figure 6b, we present such a processability map sensitive to changes in the polymer (M_w , MWD), flexibility (determined by Kuhn segment size and number), and extensibility (ratio of fully stretched chain length to coil size), and spinning conditions. The y -axis seeks to capture the influence of viscoelastic free surface flows and instabilities. In contrast, the x -axis aims to capture the impact of processing conditions like RPM and nozzle–collector distance. Here, we pick extensional relaxation time determined using capillarity-driven flows as the relevant measure. As the processing conditions and polymer type are matched, we make a pragmatic estimate for evaporation time, t_{ev} based on the value, t_{evTGA} measured using TGA but scaled down by 3600, by assuming 60 times smaller thickness than used in the TGA experiments. Here, the choice of ratios of timescales is qualitatively inspired by the operating diagram from Fang et al.¹⁵ The y -axis includes an extensional Deborah number, $De_E = \lambda_E / t_{ev}$ defined as the ratio of the extensional relaxation time to an evaporation time, t_{ev} . The x -axis choice contrasts t_{ev} and time of flight, t_{flight} .

Figure 6b, together with Table 1, suggests that the distinction between beads, beaded fibers (Figure 6c), and continuous fibers (see Figure 6d) here arises primarily due to the significant difference in the evaporation rate, for the relaxation time values change only by a factor of 2, whereas evaporation rate changes by over 12 times. A closer look at viscosity and relaxation times for aqueous solutions shows that centrifugal spinning under matched conditions does provide a jet that neither dries nor breaks into drops before reaching the collector. Increasing the distance between nozzle and collector increases time of flight, allowing centrifugal spinning from aqueous PEO solutions.¹⁰ The diameter of 5 wt. % PEO solutions is greater than 3 wt. % solutions for matched solvent composition, and the change in morphology from the mat with few beads to continuous fibers at each solvent composition (shown in Figure 2) match quite well with the regimes identified in the processability map chartered in Figure 6b.

We recognize that in centrifugal spinning (and likewise for electrospinning), solvent evaporation is influenced by the flow field within the liquid jet and the complex airflow at the jet surface. The mass loss occurs from a cylindrical filament that decreases in diameter over time, and for some cases, occurs from a cylinder that develops sinusoidal perturbations with associated variation in local evaporation rate. Additionally, we anticipate that conformational changes of the polymers in response to extensional flows that arise in spiraling jets and in necks formed between growing beads too can influence the evaporation rate. Thus, a rigorous and refined computation of t_{ev} will require careful accounting of the following: (a) mass transfer coefficient under fiber spinning conditions, which accounts for changes in jet diameter, (b) the influence of polymer conformation and concentration while the jet travels from nozzle to collector, and (c) the role of convection currents within and around the spiraling jet, and interfacial flows and instabilities, among others. Likewise, we recognize that the shear relaxation time, λ_s only quantifies the dynamics and rheology of mildly perturbed chains, and captures influence of viscoelasticity only if deformation rates are rather low. We postulate that choosing λ_E (see Figure 6b) provides a more generalized portrait that captures the influence of polymer concentration and type on response to flows with strong streamwise gradients. Nevertheless, we recognize that the deformation history, transients, and deformation rates experienced during fiber spinning need not be encountered or captured in most rheological measurements. An accurate and thorough assessment of the influence of change in polymer conformations and flow field within jets and around them on the timescales associated with instability growth, mass loss, and overall time of flight is beyond the scope of present work. We speculate that such progress would require benefit from CFS experiments with in situ analysis of concentration variation and flow fields, supplemented by computational fluid dynamics, with built-in nonlinear rheological and transport models.

We reason that the strong correlation between the measured λ_s and λ_E (see Figure 4d) only partially explains the success of the intrinsic spinnability map shown in Figure 6a, which implies linear viscoelastic response can be used to determine outcomes of a highly nonlinear process. It is well established that the interplay of capillarity and viscoelasticity determines the timescale for the growth of surface-tension-driven instabilities that drive the formation of sinusoidal beads resulting in beads or beaded fibers (see Figure 6c) as well as the late-stage evolution of fiber diameter.^{9,94,104–108,114,127–129} Studies of jetting of viscoelastic fluids show that even though linear stability analysis predicts faster breakup than expected for Newtonian fluids of the same viscosity, the preshear or unrelaxed tension effects delay the onset of sinusoidal perturbations.^{103,128,130–133} However, the drawing of jets and the late-stage pinching of necks or ligaments between beads are both influenced by extensional rheology response.^{103–106,127,129} We infer that for volatile-entangled (VE) polymer solutions, higher viscosity and unrelaxed tension contribute to a delayed appearance of sinusoidal perturbations and a rapid increase in viscosity on evaporation of volatile solvent stabilizes the jet. Furthermore, the success of operating diagrams drawn using linear viscoelastic measures (like zero shear viscosity or shear relaxation time) and experimental findings that attribute electrospinnability to the role entanglements are possibly due to the influence of high viscosity and unrelaxed tension on the suppression of instability growth in

VE solutions.^{88–91,134} We postulate an alternative, an extensibility-enriched (EE) spinnability (without need for entanglements), for ultrahigh molecular weight, relatively high extensibility polymers (like PEO, PVA, and PS). The high extensibility, flexible polymers in unentangled solutions could arise due to the strong strain hardening response and high Trouton ratios that can substantially delay pinching of necks and increase stringiness. Many published examples show that extensibility enrichment provides a pathway to make fibers from polysaccharide solutions,^{135–139} and unentangled solutions.^{30,134,140} The choice of the ordinate in Figure 6b is consistent with such extensibility-enriched spinnability, and further studies are encouraged (and underway) to explore the challenges and opportunities.

CONCLUSIONS

This paper shows that PEO fibers can be centrifugally spun using volatile-entangled (VE) solutions formulated using acetonitrile–water mixtures. We find that changing solvent properties by increasing AcN fraction influences spinnability and fiber morphology, using experiments carried out with a homebuilt CFS setup for matched rotational speed (4000 rpm), room temperature and humidity, nozzle type/size/material, and distance to the collector. We find that the intrinsic spinnability map can be outlined using two measured timescales: the shear relaxation time, determined using steady shear viscosity measured using torsional rheometry, and evaporation time, computed from the mass loss data acquired using thermogravimetric analysis (TGA). We infer that if the time of flight is long enough, a comparison of relaxation time and evaporation time facilitates the distinction between the spinnable and nonspinnable solutions. We anticipate that the intrinsic spinnability map is most suitable for the case described in this study that includes matched molecular weight and processing conditions and nearly comparable shear viscosity and shear and extensional relaxation times despite variation in AcN fraction (or solvent composition). Only evaporation rates show an order of magnitude variation for fixed polymer concentration, and hence define the benchmark for determining spinnable cases. To provide a more generalized but pragmatic portrait of spinnability, we draw a processability map that incorporates the influence of evaporation (solvent properties or ambient conditions), time of flight (RPM and nozzle–collector distance), and viscoelastic free surface flows (influenced by capillarity, elasticity, shear viscosity, and extensional rheology response) to identify spinnable formulations and distinguish between different beads, beaded fiber, and continuous fiber morphologies. In the processability map, we populate the y -axis with the ratio of extensional relaxation time to evaporation time, and the x -axis with the ratio of time of flight to evaporation time. We determined the extensional relaxation time using dripping-onto-substrate (DoS) rheometry to capture the likely influence of extensional rheology, stretched chain hydrodynamics, and viscoelastic free surface flows and instabilities. We make a pragmatic estimate for evaporation time based on the value measured using TGA. We anticipate that despite its apparent simplicity, the processability map contains information comparable to a more rigorous portrait that could be constructed by accounting for the influence of changes in polymer concentration and conformation during spinning, correlated with evaporation, instability growth and evolution, and chain relaxation timescales. Finally, we postulate that a

processability map that incorporates the influence of extensional relaxation time, evaporation time, and processing time (time of flight) can be utilized for designing and controlling volatile-entangled (VE) and extensibility-enriched (EE) spinnability, and macromolecular engineering of spinnable formulations.

AUTHOR INFORMATION

Corresponding Authors

Naveen K. Reddy – Institute for Materials Research (IMO-IMOMECE), Hasselt University, B-3590 Diepenbeek, Belgium; IMEC vzw—Division IMOMECE, B-3590 Diepenbeek, Belgium; orcid.org/0000-0003-0163-485X; Email: naveen.reddy@uhasselt.be

Vivek Sharma – Department of Chemical Engineering, University of Illinois at Chicago, Chicago, Illinois 60608, United States; orcid.org/0000-0003-1152-1285; Email: viveks@uic.edu

Authors

Jorgo Merchiers – Institute for Materials Research (IMO-IMOMECE), Hasselt University, B-3590 Diepenbeek, Belgium; IMEC vzw—Division IMOMECE, B-3590 Diepenbeek, Belgium

Carina D. V. Martínez Narváez – Department of Chemical Engineering, University of Illinois at Chicago, Chicago, Illinois 60608, United States; orcid.org/0000-0002-2356-7208

Cheryl Slykas – Department of Chemical Engineering, University of Illinois at Chicago, Chicago, Illinois 60608, United States

Complete contact information is available at:

<https://pubs.acs.org/10.1021/acs.macromol.1c01799>

Author Contributions

[†]J.M. and C.D.V.M.N. contributed equally to this work.

Notes

The authors declare no competing financial interest.

ACKNOWLEDGMENTS

J.M. and N.K.R. acknowledge IMO-IMOMECE at the University of Hasselt for providing financial support. C.D.V.M.N. acknowledges funding support by the PPG Industries, C.S. Teaching Assistantship in the Department of Chemical Engineering at UIC, and V.S. the funds from 3M nontenured faculty award (NFTA). The U. Hasselt's Packaging Technology Center is acknowledged for providing access to the tensile testing machine and Dr. Jan D'Haen for access to the SEM. The authors acknowledge discussions with students from ODES-lab students at UIC. They thank Dr. Ruth Cardinaels (Leuven, Belgium) and Dr. Samanvaya Srivasatava (UCLA) for the close reading of an early draft. V.S. acknowledges the faculty, students, and staff in Textile Technology and CPSE, Indian Institute of Technology, Delhi, for training him as an undergraduate in various aspects of manufactured fiber technology and polymer science that have contributed to the ideas in this paper (20 years later!).

REFERENCES

- (1) Atıcı, B.; Ünlü, C. H.; Yanılmaz, M. A review on centrifugally spun fibers and their applications. *Polym. Rev.* **2021**, 1–64.
- (2) Dos Santos, D. M.; Correa, D. S.; Medeiros, E. S.; Oliveira, J. E.; Mattoso, L. H. Advances in functional polymer nanofibers: From

spinning fabrication techniques to recent biomedical applications. *ACS Appl. Mater. Interfaces* **2020**, 12, 45673–45701.

- (3) Zhang, X.; Lu, Y. Centrifugal spinning: an alternative approach to fabricate nanofibers at high speed and low cost. *Polym. Rev.* **2014**, 54, 677–701.

- (4) Sarkar, K.; Gomez, C.; Zambrano, S.; Ramirez, M.; de Hoyos, E.; Vasquez, H.; Lozano, K. Electrospinning to forcespinning. *Mater. Today* **2010**, 13, 12–14.

- (5) Badrossamay, M. R.; McIlwee, H. A.; Goss, J. A.; Parker, K. K. Nanofiber assembly by rotary jet-spinning. *Nano Lett.* **2010**, 10, 2257–2261.

- (6) Rogalski, J. J.; Bastiaansen, C. W.; Peijs, T. Rotary jet spinning review—a potential high yield future for polymer nanofibers. *Nanocomposites* **2017**, 3, 97–121.

- (7) Kwak, B. E.; Yoo, H. J.; Lee, E.; Kim, D. H. Large-Scale centrifugal multispinning production of polymer micro-and nanofibers for mask filter application with a potential of cospinning mixed multicomponent fibers. *ACS Macro Lett.* **2021**, 10, 382–388.

- (8) Stojanovska, E.; Canbay, E.; Pampal, E. S.; Calisir, M. D.; Agma, O.; Polat, Y.; Simsek, R.; Gundogdu, N. S.; Akgul, Y.; Kilic, A. A review on non-electro nanofiber spinning techniques. *RSC Adv.* **2016**, 6, 83783–83801.

- (9) Park, J. H.; Rutledge, G. C. 50th anniversary perspective: advanced polymer fibers: high performance and ultrafine. *Macromolecules* **2017**, 50, 5627–5642.

- (10) Noroozi, S.; Arne, W.; Larson, R. G.; Taghavi, S. M. A comprehensive mathematical model for nanofiber formation in centrifugal spinning methods. *J. Fluid Mech.* **2020**, 892, No. A26.

- (11) Taghavi, S. M.; Larson, R. G. Regularized thin-fiber model for nanofiber formation by centrifugal spinning. *Phys. Rev. E* **2014**, 89, No. 023011.

- (12) Divvela, M. J.; Ruo, A.-C.; Zhmayev, Y.; Joo, Y. L. Discretized modeling for centrifugal spinning of viscoelastic liquids. *J. Non-Newtonian Fluid Mech.* **2017**, 247, 62–77.

- (13) Ren, L.; Ozisik, R.; Kotha, S. P.; Underhill, P. T. Highly efficient fabrication of polymer nanofiber assembly by centrifugal jet spinning: process and characterization. *Macromolecules* **2015**, 48, 2593–2602.

- (14) Noroozi, S.; Alamdari, H.; Arne, W.; Larson, R. G.; Taghavi, S. M. Regularized string model for nanofiber formation in centrifugal spinning methods. *J. Fluid Mech.* **2017**, 822, 202–234.

- (15) Fang, Y.; Dulaney, A. D.; Gadley, J.; Maia, J. M.; Ellison, C. J. Manipulating characteristic timescales and fiber morphology in simultaneous centrifugal spinning and photopolymerization. *Polymer* **2015**, 73, 42–51.

- (16) Fang, Y.; Dulaney, A. R.; Gadley, J.; Maia, J.; Ellison, C. J. A comparative parameter study: Controlling fiber diameter and diameter distribution in centrifugal spinning of photocurable monomers. *Polymer* **2016**, 88, 102–111.

- (17) Merchiers, J.; Meurs, W.; Deferme, W.; Peeters, R.; Buntinx, M.; Reddy, N. K. Influence of polymer concentration and nozzle material on centrifugal fiber spinning. *Polymers* **2020**, 12, No. 575.

- (18) Golecki, H. M.; Yuan, H.; Glavin, C.; Potter, B.; Badrossamay, M. R.; Goss, J. A.; Phillips, M. D.; Parker, K. K. Effect of solvent evaporation on fiber morphology in rotary jet spinning. *Langmuir* **2014**, 30, 13369–13374.

- (19) Veleirinho, B.; Rei, M. F.; Lopes-D.A-Silva, J. A. Solvent and concentration effects on the properties of electrospun poly (ethylene terephthalate) nanofiber mats. *J. Polym. Sci., Part B: Polym. Phys.* **2008**, 46, 460–471.

- (20) Hou, T.; Li, X.; Lu, Y.; Yang, B. Highly porous fibers prepared by centrifugal spinning. *Mater. Des.* **2017**, 114, 303–311.

- (21) Son, W. K.; Youk, J. H.; Lee, T. S.; Park, W. H. The effects of solution properties and polyelectrolyte on electrospinning of ultrafine poly (ethylene oxide) fibers. *Polymer* **2004**, 45, 2959–2966.

- (22) Fong, H.; Chun, I.; Reneker, D. H. Beaded nanofibers formed during electrospinning. *Polymer* **1999**, 40, 4585–4592.

- (23) Tripatanasuwan, S.; Zhong, Z.; Reneker, D. H. Effect of evaporation and solidification of the charged jet in electrospinning of

poly (ethylene oxide) aqueous solution. *Polymer* **2007**, *48*, 5742–5746.

(24) Pham, Q. P.; Sharma, U.; Mikos, A. G. Electrospinning of polymeric nanofibers for tissue engineering applications: a review. *Tissue Eng.* **2006**, *12*, 1197–1211.

(25) Ding, B.; Yu, J. *Electrospun Nanofibers for Energy and Environmental Applications*; Springer, 2014.

(26) Padron, S.; Patlan, R.; Gutierrez, J.; Santos, N.; Eubanks, T.; Lozano, K. Production and characterization of hybrid BEH-PPV/PEO conjugated polymer nanofibers by forcespinning. *J. Appl. Polym. Sci.* **2012**, *125*, 3610–3616.

(27) Mahalingam, S.; Edirisinghe, M. Forming of polymer nanofibers by a pressurised gyration process. *Macromol. Rapid Commun.* **2013**, *34*, 1134–1139.

(28) Jaeger, R.; Bergshoeff, M. M.; Batlle, C. M. I.; Schönherr, H.; Julius Vancso, G. *Electrospinning of Ultra-Thin Polymer Fibers*; Macromolecular Symposia; Wiley Online Library, 1998; pp 141–150.

(29) Doshi, J.; Reneker, D. H. Electrospinning process and applications of electrospun fibers. *J. Electrostat.* **1995**, *35*, 151–160.

(30) Yu, J. H.; Fridrikh, S. V.; Rutledge, G. C. The role of elasticity in the formation of electrospun fibers. *Polymer* **2006**, *47*, 4789–4797.

(31) Helgeson, M. E.; Grammatikos, K. N.; Deitzel, J. M.; Wagner, N. J. Theory and kinematic measurements of the mechanics of stable electrospun polymer jets. *Polymer* **2008**, *49*, 2924–2936.

(32) Merchiers, J.; Martínez Narváez, C. D. V.; Slykas, C.; Buntinx, M.; Deferme, W.; D'Haen, J.; Peeters, R.; Sharma, V.; Reddy, N. K. Centrifugally spun PEO fibers rival the properties of electrospun fibers. *J. Polym. Sci.* **2021**, *59*, 2754–2762.

(33) Richard-Lacroix, M.; Pellerin, C. Molecular orientation in electrospun fibers: from mats to single fibers. *Macromolecules* **2013**, *46*, 9473–9493.

(34) Barhoum, A.; Pal, K.; Rahier, H.; Uludag, H.; Kim, I. S.; Bechelany, M. Nanofibers as new-generation materials: from spinning and nano-spinning fabrication techniques to emerging applications. *Appl. Mater. Today* **2019**, *17*, 1–35.

(35) Bianco, A.; Calderone, M.; Cacciotti, I. Electrospun PHBV/PEO co-solution blends: Microstructure, thermal and mechanical properties. *Mater. Sci. Eng. C* **2013**, *33*, 1067–1077.

(36) Chavez, R. O.; Lodge, T. P.; Alcoutlabi, M. Recent developments in centrifugally spun composite fibers and their performance as anode materials for lithium-ion and sodium-ion batteries. *Mater. Sci. Eng.: B* **2021**, *266*, No. 115024.

(37) Hasan, M. T.; Gonzalez, R.; Chipara, M.; Materon, L.; Parsons, J.; Alcoutlabi, M. Antibacterial activities of centrifugally spun polyethylene oxide/silver composite nanofibers. *Polym. Adv. Technol.* **2021**, *32*, 2327–2338.

(38) Sullivan, S. T.; Tang, C.; Kennedy, A.; Talwar, S.; Khan, S. A. Electrospinning and heat treatment of whey protein nanofibers. *Food Hydrocolloids* **2014**, *35*, 36–50.

(39) Venugopal, J.; Ramakrishna, S. Applications of polymer nanofibers in biomedicine and biotechnology. *Appl. Biochem. Biotechnol.* **2005**, *125*, 147–157.

(40) Li, X.; Lu, Y.; Hou, T.; Zhou, J.; Yang, B. Centrifugally spun ultrafine starch/PEO fibres as release formulation for poorly water-soluble drugs. *Micro Nano Lett.* **2018**, *13*, 1688–1692.

(41) Samad, Y. A.; Asghar, A.; Hashaikh, R. Electrospun cellulose/PEO fiber mats as a solid polymer electrolytes for Li ion batteries. *Renewable Energy* **2013**, *56*, 90–95.

(42) Dinic, J.; Zhang, Y.; Jimenez, L. N.; Sharma, V. Extensional relaxation times of dilute, aqueous polymer solutions. *ACS Macro Lett.* **2015**, *4*, 804–808.

(43) Dinic, J.; Biagioli, M.; Sharma, V. Pinch-off dynamics and extensional relaxation times of intrinsically semi-dilute polymer solutions characterized by dripping-onto-substrate rheometry. *J. Polym. Sci., Part B: Polym. Phys.* **2017**, *55*, 1692–1704.

(44) Dinic, J.; Sharma, V. Macromolecular relaxation, strain, and extensibility determine elastocapillary thinning and extensional viscosity of polymer solutions. *Proc. Natl. Acad. Sci. U.S.A.* **2019**, *116*, 8766–8774.

(45) Dinic, J.; Sharma, V. Flexibility, extensibility, and ratio of Kuhn length to packing length govern the pinching dynamics, coil-stretch transition, and rheology of polymer solutions. *Macromolecules* **2020**, *53*, 4821–4835.

(46) Martínez Narváez, C. D. V.; Mazur, T.; Sharma, V. Dynamics and extensional rheology of polymer-surfactant association complexes. *Soft Matter* **2021**, *17*, 6116–6126.

(47) Clasen, C.; Phillips, P. M.; Palangetic, L.; et al. Dispensing of rheologically complex fluids: the map of misery. *AIChE J.* **2012**, *58*, 3242–3255.

(48) Ziabicki, A. *Fundamentals of Fibre Formation*; John Wiley & Sons: New York, 1976.

(49) Gupta, V. B.; Kothari, V. K. *Manufactured Fiber Technology*; Chapman & Hall: London, 1997.

(50) Tripathi, A.; Whittingstall, P.; McKinley, G. H. Using filament stretching rheometry to predict strand formation and “processability” in adhesives and other non-Newtonian fluids. *Rheol. Acta* **2000**, *39*, 321–337.

(51) Larson, R. G. Spinnability and viscoelasticity. *J. Non-Newtonian Fluid Mech.* **1983**, *12*, 303–315.

(52) Petrie, C. J. S. One hundred years of extensional flow. *J. Non-Newtonian Fluid Mech.* **2006**, *137*, 1–14.

(53) Dinic, J.; Jimenez, L. N.; Sharma, V. Pinch-off dynamics and dripping-onto-substrate (DoS) rheometry of complex fluids. *Lab Chip* **2017**, *17*, 460–473.

(54) Dinic, J.; Sharma, V. Power laws dominate shear and extensional rheology response and capillarity-driven pinching dynamics of entangled hydroxyethyl cellulose (HEC) solutions. *Macromolecules* **2020**, *53*, 3424–3437.

(55) Clasen, C.; Plog, J. P.; Kulicke, W. M.; Owens, M.; Macosko, C.; Scriven, L. E.; Verani, M.; McKinley, G. H. How dilute are dilute solutions in extensional flows? *J. Rheol.* **2006**, *50*, 849–881.

(56) Tirtaatmadja, V.; McKinley, G. H.; Cooper-White, J. J. Drop formation and breakup of low viscosity elastic fluids: Effects of molecular weight and concentration. *Phys. Fluids* **2006**, *18*, No. 043101.

(57) Schroeder, C. M. Single polymer dynamics for molecular rheology. *J. Rheol.* **2018**, *62*, 371–403.

(58) Somani, S.; Shaqfeh, E. S. G.; Prakash, J. R. Effect of solvent quality on the coil-stretch transition. *Macromolecules* **2010**, *43*, 10679–10691.

(59) Sasmal, C.; Hsiao, K.-W.; Schroeder, C. M.; Ravi Prakash, J. Parameter-free prediction of DNA dynamics in planar extensional flow of semidilute solutions. *J. Rheol.* **2017**, *61*, 169–186.

(60) Hsiao, K.-W.; Sasmal, C.; Ravi Prakash, J.; Schroeder, C. M. Direct observation of DNA dynamics in semidilute solutions in extensional flow. *J. Rheol.* **2017**, *61*, 151–167.

(61) Prabhakar, R.; Prakash, J. R.; Sridhar, T. Effect of configuration-dependent intramolecular hydrodynamic interaction on elastocapillary thinning and breakup of filaments of dilute polymer solutions. *J. Rheol.* **2006**, *50*, 925–947.

(62) Prabhakar, R.; Gadkari, S.; Gopesh, T.; Shaw, M. J. Influence of stretching induced self-concentration and self-dilution on coil-stretch hysteresis and capillary thinning of unentangled polymer solutions. *J. Rheol.* **2016**, *60*, 345–366.

(63) Prabhakar, R.; Sasmal, C.; Nguyen, D. A.; Sridhar, T.; Prakash, J. R. Effect of stretching-induced changes in hydrodynamic screening on coil-stretch hysteresis of unentangled polymer solutions. *Phys. Rev. Fluids* **2017**, *2*, No. 011301.

(64) Prakash, J. R. Universal dynamics of dilute and semidilute solutions of flexible linear polymers. *Curr. Opin. Colloid Interface Sci.* **2019**, *43*, 63–79.

(65) Matsumiya, Y.; Watanabe, H. Non-Universal features in uniaxially extensional rheology of linear polymer melts and concentrated solutions: A review. *Prog. Polym. Sci.* **2021**, No. 101325.

(66) Desai, P. S.; Larson, R. G. Constitutive model that shows extension thickening for entangled solutions and extension thinning for melts. *J. Rheol.* **2014**, *58*, 255–279.

- (67) Jimenez, L. N.; Dinic, J.; Parsi, N.; Sharma, V. Extensional relaxation time, pinch-off dynamics and printability of semi-dilute polyelectrolyte solutions. *Macromolecules* **2018**, *51*, 5191–5208.
- (68) Jimenez, L. N.; Martínez Narváez, C. D. V.; Sharma, V. Capillary breakup and extensional rheology response of food thickener cellulose gum (NaCMC) in salt-free and excess salt solutions. *Phys. Fluids* **2020**, *32*, No. 012113.
- (69) Martínez Narváez, C. D.; Dinic, J.; Lu, X.; Wang, C.; Rock, R.; Sun, H.; Sharma, V. Rheology and pinching dynamics of associative polysaccharide solutions. *Macromolecules* **2021**, *54*, 6372–6388.
- (70) Jimenez, L. N.; Narváez, C. D. M.; Xu, C.; Bacchi, S.; Sharma, V. The rheologically-complex fluid beauty of nail lacquer formulations. *Soft Matter* **2021**, *17*, 5197–5213.
- (71) Jimenez, L. N.; Narváez, C. D. V. M.; Xu, C.; Bacchi, S.; Sharma, V. Rheological properties influence tackiness, application and performance of nail polish/lacquer formulations. In *Surface Science and Adhesion in Cosmetics*; Wiley, 2021; pp 109–150.
- (72) Walter, A. V.; Jimenez, L. N.; Dinic, J.; Sharma, V.; Erk, K. A. Effect of salt valency and concentration on shear and extensional rheology of aqueous polyelectrolyte solutions for enhanced oil recovery. *Rheol. Acta* **2019**, *58*, 145–157.
- (73) Hsiao, K. W.; Dinic, J.; Ren, Y.; Sharma, V.; Schroeder, C. M. Passive non-linear microrheology for determining extensional viscosity. *Phys. Fluids* **2017**, *29*, No. 121603.
- (74) Marshall, K. A.; Liedtke, A. M.; Todt, A. H.; Walker, T. W. Extensional rheometry with a handheld mobile device. *Exp. Fluids* **2017**, *58*, No. 69.
- (75) Marshall, K. A.; Walker, T. W. Investigating the dynamics of droplet breakup in a microfluidic cross-slot device for characterizing the extensional properties of weakly-viscoelastic fluids. *Rheol. Acta* **2019**, *58*, 573–590.
- (76) Pack, M. Y.; Yang, A.; Perazzo, A.; Qin, B.; Stone, H. A. Role of extensional rheology on droplet bouncing. *Phys. Rev. Fluids* **2019**, *4*, No. 123603.
- (77) Suteria, N. S.; Gupta, S.; Potineni, R.; Baier, S. K.; Vanapalli, S. A. eCapillary: a disposable microfluidic extensional viscometer for weakly elastic polymeric fluids. *Rheol. Acta* **2019**, *58*, 403–417.
- (78) Xu, M.; Li, X.; Riseman, A.; Frostad, J. M. Quantifying the effect of extensional rheology on the retention of agricultural sprays. *Phys. Fluids* **2021**, *33*, No. 032107.
- (79) Su, Y.; Palacios, B.; Zenit, R. Coiling of a viscoelastic fluid filament. *Phys. Rev. Fluids* **2021**, *6*, No. 033303.
- (80) Rosello, M.; Sur, S.; Barbet, B.; Rothstein, J. P. Dripping-onto-substrate capillary breakup extensional rheometry of low-viscosity printing inks. *J. Non-Newtonian Fluid Mech.* **2019**, *266*, 160–170.
- (81) Murdoch, T. J.; Pashkovski, E.; Patterson, R.; Carpick, R. W.; Lee, D. Sticky but slick: Reducing friction using associative and nonassociative polymer lubricant additives. *ACS Appl. Polym. Mater.* **2020**, *2*, 4062–4070.
- (82) Wu, S.; Mohammadigoushki, H. Linear versus branched: flow of a wormlike micellar fluid past a falling sphere. *Soft Matter* **2021**, *17*, 4395–4406.
- (83) Franco-Gómez, A.; Onuki, H.; Yokoyama, Y.; Nagatsu, Y.; Tagawa, Y. Effect of liquid elasticity on the behaviour of high-speed focused jets. *Exp. Fluids* **2021**, *62*, No. 41.
- (84) Jafari Nodoushan, E.; Lee, Y. J.; Lee, G.-H.; Kim, N. Quasi-static secondary flow regions formed by microfluidic contraction flows of wormlike micellar solutions. *Phys. Fluids* **2021**, *33*, No. 093112.
- (85) Bird, R. B.; Armstrong, R. C.; Hassager, O. *Dynamics of Polymeric Liquids*, 2nd ed.; John Wiley & Sons: New York, 1987; Vol. 1.
- (86) Rubinstein, M.; Colby, R. H. *Polymer Physics*; Oxford University Press: New York, 2003.
- (87) Shankar, R.; Klossner, R. R.; Weaver, J. T.; Koga, T.; van Zanten, J. H.; Krause, W. E.; Colina, C. M.; Tanaka, F.; Spontak, R. J. Competitive hydrogen-bonding in polymer solutions with mixed solvents. *Soft Matter* **2009**, *5*, 304–307.
- (88) Shenoy, S. L.; Bates, W. D.; Frisch, H. L.; Wnek, G. E. Role of chain entanglements on fiber formation during electrospinning of polymer solutions: good solvent, non-specific polymer–polymer interaction limit. *Polymer* **2005**, *46*, 3372–3384.
- (89) Gupta, P.; Elkins, C.; Long, T. E.; Wilkes, G. L. Electrospinning of linear homopolymers of poly (methyl methacrylate): exploring relationships between fiber formation, viscosity, molecular weight and concentration in a good solvent. *Polymer* **2005**, *46*, 4799–4810.
- (90) Haward, S. J.; Sharma, V.; Butts, C. P.; McKinley, G. H.; Rahatekar, S. S. Shear and extensional rheology of cellulose/ionic liquid solutions. *Biomacromolecules* **2012**, *13*, 1688–1699.
- (91) McKee, M. G.; Wilkes, G. L.; Colby, R. H.; Long, T. E. Correlations of solution rheology with electrospun fiber formation of linear and branched polyesters. *Macromolecules* **2004**, *37*, 1760–1767.
- (92) Bazilevsky, A. V.; Entov, V. M.; Rozhkov, A. N. In *Liquid Filament Microrheometer and Some of Its Applications*, Third European Rheology Conference and Golden Jubilee Meeting of the British Society of Rheology, Edinburgh, U.K., 1990; Elsevier: Edinburgh, U.K., 1990; pp 41–43.
- (93) Bazilevsky, A. V.; Entov, V. M.; Rozhkov, A. N. Breakup of a liquid bridge as a method of rheological testing of biological fluids. *Fluid Dyn.* **2011**, *46*, 613–622.
- (94) McKinley, G. H. Visco-elasto-capillary thinning and break-up of complex fluids. *Rheol. Rev.* **2005**, *1*–48.
- (95) Rodd, L. E.; Scott, T. P.; Cooper-White, J. J.; McKinley, G. H. Capillary break-up rheometry of low-viscosity elastic fluids. *Appl. Rheol.* **2005**, *15*, 12–27.
- (96) Arnolds, O.; Buggisch, H.; Sachsenheimer, D.; Willenbacher, N. Capillary breakup extensional rheometry (CaBER) on semi-dilute and concentrated polyethyleneoxide (PEO) solutions. *Rheol. Acta* **2010**, *49*, 1207–1217.
- (97) Vadillo, D. C.; Mathues, W.; Clasen, C. Microsecond relaxation processes in shear and extensional flows of weakly elastic polymer solutions. *Rheol. Acta* **2012**, *51*, 755–769.
- (98) Anna, S. L.; McKinley, G. H. Elasto-capillary thinning and breakup of model elastic liquids. *J. Rheol.* **2001**, *45*, 115–138.
- (99) Campo-Deaño, L.; Clasen, C. The slow retraction method (SRM) for the determination of ultra-short relaxation times in capillary breakup extensional rheometry experiments. *J. Non-Newtonian Fluid Mech.* **2010**, *165*, 1688–1699.
- (100) Morozova, S.; Schmidt, P. W.; Metaxas, A.; Bates, F. S.; Lodge, T. P.; Dutcher, C. S. Extensional flow behavior of methylcellulose solutions containing fibrils. *ACS Macro Lett.* **2018**, *7*, 347–352.
- (101) Wagner, C.; Amarouchene, Y.; Bonn, D.; Eggers, J. Droplet detachment and satellite bead formation in viscoelastic fluids. *Phys. Rev. Lett.* **2005**, *95*, No. 164504.
- (102) Sattler, R.; Gier, S.; Eggers, J.; Wagner, C. The final stages of capillary break-up of polymer solutions. *Phys. Fluids* **2012**, *24*, No. 023101.
- (103) Yarin, A. L. *Free Liquid Jets and Films: Hydrodynamics and Rheology*; Longman Scientific & Technical: New York, 1993.
- (104) Sharma, V.; Haward, S. J.; Serdy, J.; Keshavarz, B.; Soderlund, A.; Threlfall-Holmes, P.; McKinley, G. H. The rheology of aqueous solutions of Ethyl Hydroxy-Ethyl Cellulose (EHEC) and its hydrophobically modified Analogue (hmEHEC): Extensional flow response in capillary break-up, jetting (ROJER) and in a cross-slot extensional rheometer. *Soft Matter* **2015**, *11*, 3251–3270.
- (105) Sharma, V.; Ardekani, A. M.; McKinley, G. H. In “Beads on a String” Structures and Extensional Rheometry Using Jet Break-Up, 5th Pacific Rim Conference on Rheology (PRCR-5); Australian Society of Rheology, 2010.
- (106) Ardekani, A.; Sharma, V.; McKinley, G. H. Dynamics of bead formation, filament thinning and breakup of weakly viscoelastic jets. *J. Fluid Mech.* **2010**, *665*, 46–56.
- (107) Greiciunas, E.; Wong, J.; Gorbatenko, I.; Hall, J.; Wilson, M. C. T.; Kapur, N.; Harlen, O. G.; Vadillo, D.; Threlfall-Holmes, P. Design and operation of a Rayleigh Ohnesorge jetting extensional rheometer (ROJER) to study extensional properties of low viscosity polymer solutions. *J. Rheol.* **2017**, *61*, 467–476.

- (108) Mathues, W.; Formenti, S.; McIlroy, C.; Harlen, O. G.; Clasen, C. CaBER vs ROJER-Different time scales for the thinning of a weakly elastic jet. *J. Rheol.* **2018**, *62*, 1135–1153.
- (109) Entov, V. M.; Hinch, E. J. Effect of a spectrum of relaxation times on the capillary thinning of a filament of elastic liquid. *J. Non-Newtonian Fluid Mech.* **1997**, *72*, 31–54.
- (110) Zhou, J.; Doi, M. Dynamics of viscoelastic filaments based on Onsager principle. *Phys. Rev. Fluids* **2018**, *3*, No. 084004.
- (111) Wagner, C.; Bourouiba, L.; McKinley, G. H. An analytic solution for capillary thinning and breakup of FENE-P fluids. *J. Non-Newtonian Fluid Mech.* **2015**, *218*, 53–61.
- (112) Eggers, J.; Herrada, M. A.; Snoeijer, J. H. Self-similar breakup of polymeric threads as described by the Oldroyd-B model. *J. Fluid Mech.* **2020**, *887*, No. A19.
- (113) Deblais, A.; Herrada, M. A.; Eggers, J.; Bonn, D. Self-similarity in the breakup of very dilute viscoelastic solutions. *J. Fluid Mech.* **2020**, *904*, No. R2.
- (114) Bhat, P. P.; Appathurai, S.; Harris, M. T.; Pasquali, M.; McKinley, G. H.; Basaran, O. A. Formation of beads-on-a-string structures during break-up of viscoelastic filaments. *Nat. Phys.* **2010**, *6*, 625–631.
- (115) Larson, R. G. *Constitutive Equations for Polymer Solutions and Melts*; Butterworth Publishers: Boston, 1988.
- (116) Yaoita, T.; Isaki, T.; Masubuchi, Y.; Watanabe, H.; Ianniruberto, G.; Marrucci, G. Primitive chain network simulation of elongational flows of entangled linear chains: Role of finite chain extensibility. *Macromolecules* **2011**, *44*, 9675–9682.
- (117) Yaoita, T.; Isaki, T.; Masubuchi, Y.; Watanabe, H.; Ianniruberto, G.; Marrucci, G. Primitive chain network simulation of elongational flows of entangled linear chains: Stretch/orientation-induced reduction of monomeric friction. *Macromolecules* **2012**, *45*, 2773–2782.
- (118) Bobbili, S. V.; Milner, S. T. Chain tension reduces monomer friction in simulated polymer melts. *J. Rheol.* **2020**, *64*, 1373–1378.
- (119) Kushwaha, A.; Shaqfeh, E. S. G. Slip-link simulations of entangled polymers in planar extensional flow: Disentanglement modified extensional thinning. *J. Rheol.* **2011**, *55*, 463–483.
- (120) Ye, X.; Larson, R. G.; Pattamaprom, C.; Sridhar, T. Extensional properties of monodisperse and bidisperse polystyrene solutions. *J. Rheol.* **2003**, *47*, 443–468.
- (121) Rasmussen, H. K.; Wingstrand, S. L.; Hassager, O. On the universality in the extensional rheology of monodisperse polymer melts and oligomer dilutions thereof. *Rheol. Acta* **2019**, *58*, 333–340.
- (122) Huang, Q.; Hengeller, L.; Alvarez, N. J.; Hassager, O. Bridging the gap between polymer melts and solutions in extensional rheology. *Macromolecules* **2015**, *48*, 4158–4163.
- (123) Huang, Q.; Mednova, O.; Rasmussen, H. K.; Alvarez, N. J.; Skov, A. L.; Almdal, K.; Hassager, O. Concentrated polymer solutions are different from melts: Role of entanglement molecular weight. *Macromolecules* **2013**, *46*, 5026–5035.
- (124) Sharma, V.; Song, L.; Jones, R. L.; Barrow, M. S.; Williams, P. R.; Srinivasarao, M. Effect of solvent choice on breath-figure-templated assembly of. *EPL (Europhys. Lett.)* **2010**, *91*, No. 38001.
- (125) Crank, J. *The Mathematics of Diffusion*, 2nd ed.; Oxford University Press, 1979.
- (126) Eggers, J. Nonlinear dynamics and breakup of free-surface flows. *Rev. Mod. Phys.* **1997**, *69*, 865–929.
- (127) Clasen, C.; Eggers, J.; Fontelos, M. A.; Li, J.; McKinley, G. H. The beads-on-a-string structure of viscoelastic threads. *J. Fluid Mech.* **2006**, *556*, 283–308.
- (128) Middleman, S. Stability of a viscoelastic jet. *Chem. Eng. Sci.* **1965**, *20*, 1037–1040.
- (129) Bousfield, D. W.; Keunings, R.; Marrucci, G.; Denn, M. M. Nonlinear analysis of the surface tension driven breakup of viscoelastic filaments. *J. Non-Newtonian Fluid Mech.* **1986**, *21*, 79–97.
- (130) Goldin, M.; Yerushalmi, J.; Pfeffer, R.; Shinnar, R. Breakup of a laminar capillary jet of a viscoelastic fluid. *J. Fluid Mech.* **1969**, *38*, 689–711.
- (131) Bazilevskii, A. V.; Entov, V. M.; Rozhkov, A. N. Elastic stresses in capillary jets of dilute polymer solutions. *Fluid Dyn.* **1985**, *20*, 169–175.
- (132) Mun, R. P.; Byars, J. A.; Boger, D. V. The effects of polymer concentration and molecular weight on the breakup of laminar capillary jets. *J. Non-Newtonian Fluid Mech.* **1998**, *74*, 285–297.
- (133) Goren, S. L.; Gottlieb, M. Surface-tension-driven breakup of viscoelastic liquid threads. *J. Fluid Mech.* **1982**, *120*, 245–266.
- (134) Palangetic, L.; Reddy, N. K.; Srinivasan, S.; Cohen, R. E.; McKinley, G. H.; Clasen, C. Dispersity and spinnability: Why highly polydisperse polymer solutions are desirable for electrospinning. *Polymer* **2014**, *55*, 4920–4931.
- (135) Rošic, R.; Pelipenko, J.; Kocbek, P.; Baumgartner, S.; Bešter-Rogač, M.; Kristl, J. The role of rheology of polymer solutions in predicting nanofiber formation by electrospinning. *Eur. Polym. J.* **2012**, *48*, 1374–1384.
- (136) Mengistu Lemma, S.; Bossard, F.; Rinaudo, M. Preparation of pure and stable chitosan nanofibers by electrospinning in the presence of poly (ethylene oxide). *Int. J. Mol. Sci.* **2016**, *17*, No. 1790.
- (137) Mirtič, J.; Balažic, H.; Zupančič, Š.; Kristl, J. Effect of solution composition variables on electrospun alginate nanofibers: Response surface analysis. *Polymers* **2019**, *11*, No. 692.
- (138) Rieger, K. A.; Birch, N. P.; Schiffman, J. D. Electrospinning chitosan/poly (ethylene oxide) solutions with essential oils: Correlating solution rheology to nanofiber formation. *Carbohydr. Polym.* **2016**, *139*, 131–138.
- (139) Pakravan, M.; Heuzey, M.-C.; Aji, A. A fundamental study of chitosan/PEO electrospinning. *Polymer* **2011**, *52*, 4813–4824.
- (140) Malkin, A. Y.; Semakov, A. V.; Skvortsov, I. Y.; Zatonikhin, P.; Kulichikhin, V. G.; Subbotin, A. V.; Semenov, A. N. Spinnability of dilute polymer solutions. *Macromolecules* **2017**, *50*, 8231–8244.